ANNUAL REVIEWS

Annual Review of Materials Research

First-Principles Calculations of Point Defects for Quantum Technologies

Cyrus E. Dreyer,[1] Audrius Alkauskas,[2] John L. Lyons,[3] Anderson Janotti,[4] and Chris G. Van de Walle[5]

[1]Department of Physics and Astronomy, Rutgers University, Piscataway, New Jersey 08854-8019, USA; email: cedreyer@physics.rutgers.edu

[2]Center for Physical Sciences and Technology, LT-10257 Vilnius, Lithuania

[3]Center for Computational Materials Science, United States Naval Research Lab, Washington, DC 20375-0001, USA

[4]Department of Materials Science and Engineering, University of Delaware, Newark, Delaware 19716-3106, USA

[5]Materials Department, University of California, Santa Barbara, California 93106-5050, USA

Annu. Rev. Mater. Res. 2018. 48:2.1–2.26

The *Annual Review of Materials Research* is online at matsci.annualreviews.org

https://doi.org/10.1146/annurev-matsci-070317-124453

Keywords

point defects, quantum computing, quantum metrology, quantum communication, single-photon emitters, density functional theory

Abstract

Point defects in semiconductors and insulators form an exciting system for realizing quantum technologies, including quantum computing, communication, and metrology. Defects provide a platform that combines the environmental isolation necessary to maintain the coherence of quantum states with the ability to perform electrical and optical manipulation. First-principles calculations play a crucial role in identifying, characterizing, and developing defects for quantum applications. We review the first-principles methodologies for calculating the relevant structural, electronic, vibrational, optical, and magnetic properties of defects for quantum technologies. We illustrate the utility and accuracy of these techniques by using examples from the literature. We also point out areas in which further development of the computational techniques is desirable.

1. INTRODUCTION

Since it was first theorized that a computer based on a quantum system would be able to surpass fundamental limitations on classical computers (1), there has been vigorous interest in the manipulation of systems that exhibit quantum-mechanical effects. To date there have been proposals for using quantum effects in technologies such as computing, communication, and metrology. Exploiting the unique properties of quantum mechanics for technological applications is very challenging, however. The system must be isolated from the environment to maintain the coherence of the quantum states but still allow for manipulation and readout.

A number of systems have been proposed and (to varying extents) developed to realize quantum technologies, including atoms (2), superconducting circuits (3), and quantum dots (4). Point defects in semiconductors and insulators form a promising paradigm in which the often contradictory properties of isolation and access can be reconciled. Throughout this review, we use the term point defects to refer either to intrinsic imperfections in the crystal lattice (vacancies, interstitials, or antisites) or to impurity atoms incorporated into the lattice, as well as to complexes involving either or both. By semiconductors and insulators, we are referring to materials that have band gaps (i.e., not metals). The term semiconductors usually refers to materials such as Si, Ge, and GaAs, whose conductivity can be well controlled via doping, while the term insulators refers to materials that exhibit very high resistivity. Traditionally, the delineation between these two classes was based on the magnitude of the band gap. However, progress in the field of wide-band-gap (and ultrawide-band-gap) semiconductors has blurred this distinction, and doping of some materials with band gaps exceeding 6 eV (such as AlN or BN) has been demonstrated.

Point defects can act as artificial atoms embedded in the medium of the material, which isolates them from one another and, to some extent, from the environment; therefore, they exhibit quantum properties of isolated atoms without the necessity for complex isolation techniques such as ion traps or optical lattices (2). The solid-state framework of defects is also beneficial for scalability and incorporation into devices, and the accumulated knowledge from decades of point-defect research can be leveraged for design, fabrication, identification, and manipulation.

The application of point defects has already been demonstrated in the context of several quantum technologies, such as quantum bits (qubits) for quantum computation (5), single-photon emitters (SPEs) for quantum communication (6), and nanoscale sensors for quantum metrology (7). However, there are still significant fundamental as well as technological challenges to their further development, including limited exploration of candidate defects and host materials that satisfy the necessary criteria for quantum applications (8), and there is an incomplete understanding of important processes even in well-characterized defects (9).

First-principles calculations provide powerful tools for exploring the properties of defects in semiconductors and insulators. State-of-the-art techniques allow for quantitative prediction of the electronic and atomic structure, as well as optical and magnetic properties (see Reference 10 for a review). Comparison of these predictions with experiment enables defect identification as well as an assessment of the suitability for device applications.

The main goal of this review is to address these computational methods for determining defect properties. We do so in the context of point defects for quantum technologies, an emerging application area of rising interest; many of the techniques we discuss also have broader applications in the field of point defects. The structure of this review is as follows. In Section 2 we outline both how defects can be used in various quantum technologies and the relevant and desirable properties in each case. In Section 3 we introduce the various first-principles methods relevant for defect calculations. In Section 4 we discuss how these methods can be applied to calculate the defect properties relevant for applications. Section 5 contains a summary and outlook.

2. POINT DEFECTS FOR QUANTUM APPLICATIONS

2.1. Defects as Spin Qubits

Quantum computing is one of the most exciting, yet most challenging, quantum technologies (11). A quantum computer is a device that uses quantum entanglement and superposition to perform computational tasks. The idea that the laws of quantum mechanics could be used in computation or, more generally, in information processing dates back to the 1980s. In particular, Yuri Manin, Richard Feynman, and others realized that the physics of systems in which quantum entanglement plays a role cannot be efficiently simulated using classical computers (11). This suggested the idea of alternative ways to process information, eventually giving rise to a completely new field, that of quantum information science (11).

The central component of a quantum computer is a qubit. This is a two-level system with states that could be labeled $|0\rangle$ and $|1\rangle$. The system can exist in a coherent superposition of these two states for a duration that is termed the coherence time, T_2. The quantum state of a qubit can be entangled with that of other qubits, creating nonlocal correlations that are at the core of quantum computing. The key metric of a quantum computer is the number of single- and two-qubit gate operations that can be applied before the quantum-mechanical state decoheres.

A number of physical systems have been investigated as potential qubits (see Reference 12 for a review). Among these, utilizing the spin states of point defects in semiconductors and insulators is a promising avenue for realizing scalable and robust qubits (8). One important technology is related to spin qubits associated with phosphorus donors in silicon (13), a spin-1/2 system. The two spin sublevels can be split in an external magnetic field, enabling an electrical initialization and readout of the spin. Impressive advances in the field of silicon donor qubits (5, 14, 15) have partly been enabled by the maturity of the silicon technological platform. Since phosphorous is a shallow donor, the operation of these qubits requires cryogenic temperatures to avoid ionization; the qubit cannot function if the electron is thermally excited to the conduction band and no longer bound to the P atom.

A different path toward defects as spin qubits is provided by point defects in wide-band-gap semiconductors. Here, defects with deep levels are employed, meaning that the defect levels are far away from the band edges (typically by at least 0.5 eV), and the corresponding wave functions are localized on the scale of atomic bond lengths (as opposed to the wave functions associated with shallow dopants, which can be tens or even hundreds of angstroms in extent). The larger energy scales make electrical manipulation of the state of the defect more challenging, and spin initialization is achieved via optical means. The prototype point-defect qubit is the negatively charged nitrogen-vacancy (NV^-) center in diamond (see Reference 9 for a review). This defect consists of a substitutional nitrogen next to a vacant site, as shown in **Figure 1*a***. Building on significant early studies of the properties of NV^- in ensembles of defects [e.g., by Davies (16)], the detection of single NV centers in 1997 (17) was a seminal achievement that sparked the interest in the field.

The usefulness of the NV^- center as a spin qubit stems from its electronic structure, shown in **Figure 1*b*,*c***. The ground-state occupation of single-particle states for the negative charge state is shown in **Figure 1*b*** (methods for calculating such states are discussed in Sections 4.1 and 4.2). The defect has two singly degenerate states with a_1 symmetry that are filled (the lower one is resonant with the valence band) and a doubly degenerate state with e symmetry that is half filled. The resulting ground state is a triplet $^3A_2$ state (**Figure 1*c***). The $m_s = 0$ and $m_s = \pm 1$ magnetic sublevels have a so-called zero-field splitting (ZFS) of $D = 2.88$ GHz (9) (see Section 4.5). The defect can be optically excited to the ^3E state by exciting an electron from the upper a_1 state to

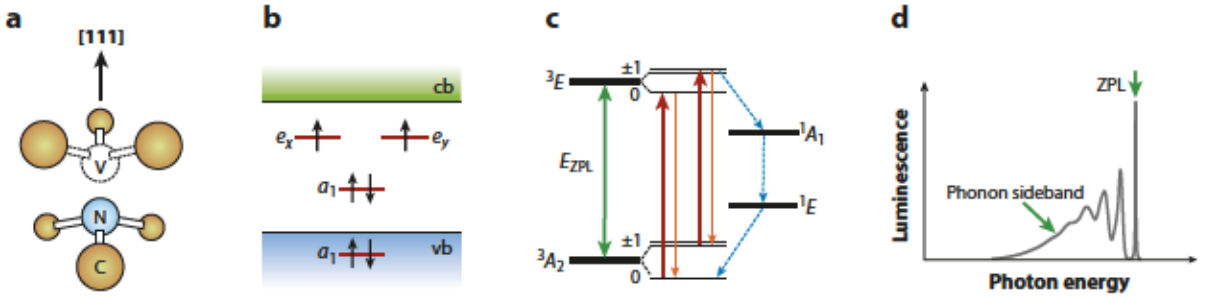

Figure 1

(*a*) The atomic structure of the nitrogen-vacancy (NV^-) center in diamond. Carbon atoms (C) are light brown, the nitrogen atom (N) is blue, and the vacancy site (V) is indicated by a dashed circle. (*b*) Schematic of the single-particle states associated with the NV^- defect, positioned relative to the conduction band (cb) and valence band (vb) of diamond. The labels refer to the irreducible representations. (*c*) The mechanism of spin initialization via optical excitation, as described in the text. Red solid lines denote optical excitations; orange solid lines denote optical emission, with the thinner line between the $m_s = 1$ sublevels indicating the reduced intensity resulting from competition with the intersystem crossing (*blue dashed lines*). (*d*) A schematic of the luminescence band of NV^- centers. It is composed of the zero-phonon line (ZPL) and the phonon side band.

an empty e state, and the zero-phonon line (ZPL) of the transition is 1.945 eV (637 nm) (see also Section 4.3). At room temperature the excited state possesses a similar structure of magnetic sublevels with a ZFS of $D = 1.42$ GHz (9). Optical excitation (**Figure 1*c***) is mostly spin preserving, meaning that the $m_s = 0$ level of the ground state couples to the $m_s = 0$ level of the excited state, and likewise for $m_s = \pm 1$ levels.

Besides the triplet states, there exist two low-lying singlet states, $^1A_1$ and ^1E. If the system is initially in the $m_s = 0$ level of the excited ^3E state, it returns to the ground state via emission of a photon with a lifetime of ~13 ns. However, for the $m_s = \pm 1$ states there is a comparable probability for the so-called intersystem crossing (ISC), whereby the NV^- center transitions into the singlet $^1A_1$ state. After that, there is a very fast (lifetime ~1 ns, mostly nonradiative) transition to the lower-lying ^1E state. This is a relatively long-lived metastable state [lifetime of ~150 ns at room temperature (18)]. From here the system undergoes another ISC to the triplet $^3A_2$ state, predominantly coupling to the $m_s = 0$ sublevel. After a few such cycles, the NV^- center can be initialized into the $m_s = 0$ spin state, which can then be controlled using microwaves. The electronic structure of the NV^- center thus enables optical spin initialization. Conveniently, it also allows for optical spin readout, as the luminescence intensity now depends on the spin state (**Figure 1*b***). The above-described mechanism of spin initialization and readout has been understood after many years of experimental research (9), with the upper ISC put on firm theoretical ground (19).

In contrast to the case for silicon, which has a well-developed technological platform, growth and fabrication of diamond-based devices are much less developed. This difficulty has motivated scientists to search for other wide-band-gap semiconductors that could potentially host NV^- analogs (8). SiC was a natural choice, and a few defects have been suggested as promising candidates (20, 21). One prominent defect is the neutral divacancy $(V_C\text{-}V_{Si})^0$, for which a number of impressive advances, including the detection of single centers with millisecond coherence times, have been demonstrated (22). An additional advantage of SiC is that it is available in several polytypes, including hexagonal (4*H* and 6*H*) and cubic (3*C*), all of which have slightly different defect properties (23). One major outstanding challenge in using deep defects in diamond and SiC as spin qubits is how to efficiently couple distant spins, a topic of current research.

2.2. Defects as Single-Photon Emitters

In Section 2.1, we describe situations in which the spin of the defect was the quantum system used in information processing. A different path is to use the quantum properties of photons instead; this defines an active topic of research under the general descriptor of quantum photonic technologies or quantum photonics (24). The distinguishing feature of quantum photonics is that the behavior of light cannot be understood only in terms of the classical description provided by Maxwell's equations. The light can take several forms, e.g., in the form of so-called squeezed states or even semiclassical coherent states that are generated by a laser (24). Many ideas for future technologies that will make use of the quantum nature of light require single photons. Those are produced by SPEs, which occupy a special place in photonic quantum technologies.

An SPE is a physical system that emits one photon with a well-defined frequency and polarization in a (more or less) deterministic fashion. A few distinct quantum technologies can make use of these nonclassical light sources (see Reference 25 for a review). One idea is that of optical quantum computing, whereby a qubit is encoded in a single photon with states $|0\rangle$ (no photon) or $|1\rangle$ (one photon). In principle a universal quantum computer can be built using photons as qubits, similar to the silicon or diamond quantum computer discussed above.

SPEs also play a key role in quantum communication (26). Some protocols of quantum communication, even those that in principle do not require single photons, are absolutely secure only in the single-photon limit (26), while others require the use of single photons by construction (27).

Single-photon emission has been realized in a few distinct physical systems. The requirements for an ideal SPE have been summarized by Aharonovich and coworkers (6, 25). At the moment no single system meets all the requirements, and the best realization is yet to emerge. Point defects in solids have emerged as a very promising platform, with leading candidates being point defects in diamond (6) such as the above-mentioned NV^- center and the silicon-vacancy (SiV) center. The luminescence spectrum of the NV^- center is composed of the ZPL and a phonon side band, as shown in **Figure 1*c*** (see Section 4.3). The contribution of the luminescence intensity relative to the total integrated intensity is the Debye-Waller (DW) factor. At low temperatures the experimental DW factor for NV^- is approximately 3% (28), and its value decreases with increasing T. This is an important parameter since only ZPL photons have well-defined frequency and polarization. Another important criterion is the quantum efficiency of the center as an optical emitter, which is defined as the radiative rate divided by the overall (radiative plus nonradiative) rate. The quantum efficiency of the NV^- center is less than 0.7 due to the existence of the ISC, discussed in Section 2.1. An additional shortcoming of the NV center is that it possesses electric dipole moments in both the excited and the ground state, making the transition energy sensitive to local electric fields. Since electric fields tend to fluctuate across the sample, no two NVs are absolutely identical. Overall, then, the NV center itself is far from an ideal SPE. However, many interesting and informative proof-of-principle experiments have been performed with NV centers, and hence they continue to be used as a prototype SPE.

The negatively charged SiV^- center in diamond overcomes many of the difficulties associated with the NV center. Due to the large size mismatch between Si and C, the Si atom is significantly displaced from its nominal lattice site, effectively occupying a site midway between two vacancies. As a result, the center has inversion symmetry. This implies that the interaction with even-symmetry phonons is not allowed during optical transitions, reducing the intensity of the phonon side band and rendering the DW factor as high as 70% (29). The existence of the inversion center also means that there is no net electric dipole moment, making the SiV center much less susceptible to electric fields. These features have allowed for a demonstration of indistinguishability of

two separated SiV centers (30). Unfortunately, the quantum efficiency of SiV centers is believed to be lower than that of NV centers, of the order of [illegible] which is certainly not ideal.

Similar to the case of spin qubits, the difficulties relating to SPEs in diamond have motivated a search for SPEs in other materials. In 2012 an SPE was detected in a laser material, yttrium aluminum garnet (31). Impressive progress has also been made in silicon carbide, with the first SPE detected in 2014 (32); subsequent achievements were reviewed in Reference 33. Other materials in which defect-related single-photon emission has been reported include hexagonal boron nitride, transition metal dichalcogenides (WSe_2 and MoS_2), zinc oxide, and gallium nitride (25).

The grouping of point defects as either spin qubits (Section 2.1) or SPEs (Section 2.2) has been chosen mainly for convenience. Clearly, some defects, such as the NV center, can act as both. The NV center can generate single photons with a defined quantum-mechanical state, and it can also host a spin that can be prepared in a given state. This creates a spin-photon interface, where the state of a photon can be mapped onto a spin, and vice versa. Spin-photon interfaces are important for a number of quantum technologies (34).

2.3. Defects for Metrology

Point defects can be used as sensors of an external physical parameter. Once calibrated, a specific spectroscopic signature of a point defect that depends on that measured parameter provides a good metrology tool. The famous R-line of Cr^{3+} in Al_2O_3 (ruby) provides a very good example. This narrow line, with a wavelength of 694.3 nm at room temperature (35), is easily observed in fluorescence and gives ruby its dark red color. It is caused by the transition between the first excited state, ^2E, and the ground state, $^4A_2$. The optical transition requires a spin flip and is therefore slow (with a lifetime of a few milliseconds). The sensitive temperature dependence of the wavelength, line width (35), and lifetime (36) of the R-line can be used for temperature measurement. Similarly, the wavelength of the line is sensitive to the external pressure. This sensitivity can be used for pressure measurements in otherwise inaccessible high-pressure environments, such as inside a diamond anvil cell (37).

More important in the current context is the ability to use single defects as sensors, as this provides nanometer-scale spatial resolution. The NV^- center in diamond plays a prominent role here (7), having given birth to the field of defect nanometrology. NV^- centers have been demonstrated as sensors of magnetic and electric fields, strain, pressure, and temperature (7). For example, the dependence of the ZFS on temperature can be used to construct NV^- thermometers (38). Also, the $m_s = \pm 1$ spin sublevels (**Figure 1*a***) are degenerate in the absence of an external magnetic field and split when a magnetic field is applied; probing this splitting with continuous-wave optically detected magnetic resonance (ODMR) offers a way to accurately measure magnetic-field strength (39) (see Section 4.5).

Continuous-wave experiments build on classical spectroscopic techniques (albeit with possible nanoscale resolution) and thus cannot be considered a quantum technology, since quantum-mechanical coherence of states does not directly enter into the measurement protocol. Sensitivity to external parameters can be significantly enhanced in pulsed experiments, in which spin coherence in the ground state is utilized (7) through interferometry of the quantum states (e.g., NV after spin state). Pulsed experiments are similar to continuous-wave techniques in that they measure the change in the ground-state magnetic-level structure; however, such measurement is done indirectly, using a variety of microwave protocols that have been developed in the field of magnetic resonance. One common protocol is a Ramsey experiment, in which one $\pi/2$ pulse puts the system into a coherent superposition of the two chosen magnetic sublevels, inducing a precession of the spin. After some time another $\pi/2$ pulse is applied, and the spin is read out via

fluorescence. The precession depends on the external magnetic field, providing a measurement of magnetic field strength (40). Similar techniques can be used to measure other parameters, such as temperature (41).

We emphasize that the field of nanometrology is not limited to NV centers in diamond. Defects in SiC hold similar potential (42), and many more defect spin qubits and SPEs can be considered.

3. ELECTRONIC STRUCTURE METHODS

Electronic structure theory plays a fundamental role in determining the properties of matter, including cohesive energy, equilibrium crystal structure, thermodynamic properties, phase transitions, electronic and heat transport, magnetism, ferroelectricity, and the properties of defects in crystalline solids (43). Electronic structure is based on the laws of quantum mechanics to describe the movement and distribution of the electrons in an external potential. A solid is a system of electrons moving in an external field given by the Coulomb potential of the nuclei, and all the physical information is contained in the many-body wave function, which depends on the coordinates of all the electrons and the nuclei. In a first approximation, we can separate the motion of the electrons from that of the nuclei; this is the Born-Oppenheimer approximation (43, 44), which rests on the fact that the nuclei are much heavier than the electrons, and it is equivalent to writing the total wave function as a product of a wave function that depends on the coordinates of the nuclei and another that depends on the coordinates of the electrons and only parametrically on the coordinates of the nuclei. This separation results in an equation that represents the movement of the electrons in the field created by fixed ions. Solving the equation for the electrons is still a daunting task for many-electron systems because it involves the coordinates of each electron and the equation cannot be further separated into a set of equations for each electron because of the Coulomb interaction between the electrons.

The many-electron equation for a solid can, in principle, be solved by the Hartree-Fock method (45), in which the many-electron wave function is approximated by a Slater determinant involving products of single-electron wave functions. The problem with the Hartree-Fock method is that it does not include electronic correlations, leading to large errors in lattice parameters of crystalline solids, overestimation of band gaps of semiconductors and insulators, and anomalies in the electronic structure of metals near the Fermi energy (43).

Density functional theory (DFT) constitutes a completely different approach to the problem, in which the many-electron wave function is no longer the central quantity. DFT, which is presently the most successful and efficient approach for computing the electronic structure of solids (43), was put on a firm theoretical footing in a seminal paper by Hohenberg & Kohn (46). They demonstrated that the ground-state properties of a many-electron system are uniquely determined by an electron density that depends on only three spatial coordinates, thus laying the groundwork for reducing the many-body problem of N electrons with $3N$ spatial coordinates to three spatial coordinates through the use of a functional of the electron density. That is, the ground-state total energy of a system of N electrons is a functional of the density.

Kohn & Sham (47) subsequently provided a methodology for efficiently solving for the ground-state density by considering an auxiliary system of single-particle orbitals whose ground-state density is the same as the interacting many-body density. Their expression for the energy is a sum of the kinetic energy of noninteracting electrons; the classical Coulomb repulsion between the electrons (the Hartree term); the potential energy of the electrons in the field of the nuclei; and the so-called exchange and correlation energy, which contains the explicitly quantum-mechanical interactions between the electrons and can be expressed as a functional of the electron density. Using the variational principle, one can minimize the total energy with respect to the single-particle

orbitals and obtain the Kohn-Sham equation, which looks just like a single-particle Schrödinger equation. The exact form of the exchange-correlation potential is not known, but approximate forms have been developed, for which we can solve the Kohn-Sham equations self-consistently.

Finding a computationally efficient yet physical approximation to the exchange-correlation term has remained a central problem in DFT. One of the earliest and still widely used forms is the local density approximation (LDA), which is a local functional of the density (47) fitted [e.g., by Perdew & Zunger (48)] to reproduce accurate quantum Monte Carlo calculations for the homogeneous electron gas performed by Ceperley & Alder (49). An extension of the LDA is to include a dependence on the derivative of the charge density, in the so-called generalized gradient approximation (GGA) [e.g., the widely used PBE functional of Perdew, Burke, and Ernzerhof (50)]. The latter approximation has been widely used to describe many ground-state properties of solids with great success, including lattice parameters, elastic constants, phonon spectra, stability of different phases, phase transformation under pressure, enthalpies of reactions, interfaces, and surface reconstructions.

A well-known deficiency of DFT within the local (LDA) or semilocal (GGA) approximations is that they severely underestimate the band gap of semiconductors and insulators (51, 52). These functionals suffer from an artificial self-interaction; i.e., the interaction of an electron with itself is not excluded from the equations, as it would be in a Hartree-Fock approach. The LDA and GGA exchange-correlation functionals lack a derivative discontinuity at integer occupancies, in particular for the highest-energy occupied and lowest-energy unoccupied states that define the band gap in semiconductors or insulators (53, 54). One way to (partially) correct for this spurious interaction is to include a nonlocal Hartree-Fock exchange term. Mixing nonlocal Fock exchange with the GGA exchange, in a so-called hybrid functional (55, 56), leads to significant improvements in the description of band gaps. The Heyd-Scuseria-Ernzerhof (HSE06) hybrid functional (57) is very successful in describing band gaps and structural parameters of a wide range of materials systems. This hybrid functional approach is much more computationally expensive than LDA or GGA, restricting the size of systems that can be treated. Significantly, the corrections to the band gap obtained by using a hybrid functional do not simply amount to a rigid upward shift of the conduction band; both the valence band (determining the ionization potential) and the conduction band (determining the electron affinity) are affected. For instance, in ZnO the correction to the valence and conduction bands is 65%/35% (58), as schematically shown in **Figure 2**. In comparison to semilocal functionals, hybrid functionals offer a much better treatment of localized electronic states, which is very important in the description of defect wave functions (10). In the past decade or so, hybrid functionals have become the standard tool with which to calculate the properties of point defects in semiconductors (10, 59), including defects for quantum technologies.

4. FIRST-PRINCIPLES CALCULATIONS OF POINT DEFECTS

In Section 2 we outline how defects can be used for quantum technologies. In the current section we show how first-principles calculations play two crucial roles in the development of such technologies.

The first role is to enable identification of defects and to build an understanding of defect properties. Identifying the microscopic origin of experimentally observed signals is often extremely difficult. First-principles calculations can generate information that can be directly matched with experiment, thus unambiguously determining the atomic structure and chemical nature of the defect. For instance, in Section 4.3 we show how calculated photoluminescence (PL) line shapes can be compared with experimental spectra, and in Section 4.5 we outline how magnetic properties of defects can be compared to ODMR measurements. First-principles calculations of excited-state

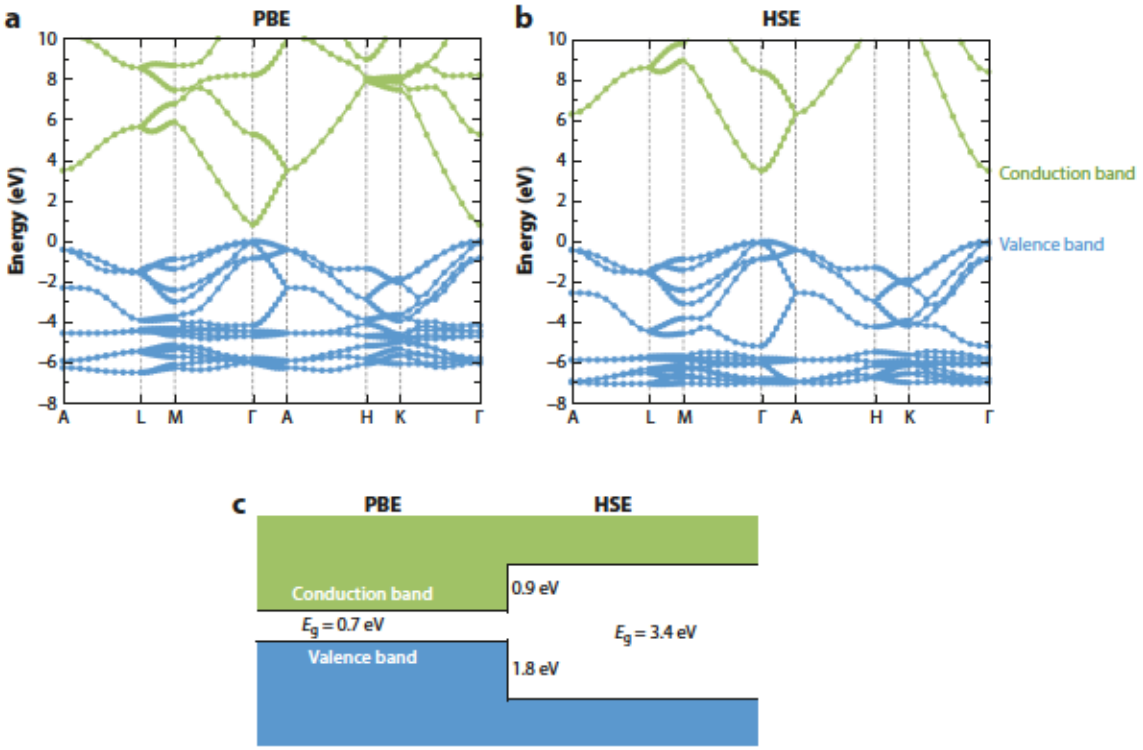

Figure 2

(*a*,*b*) Calculated electronic band structure of ZnO using (*a*) the PBE (Perdew-Burke-Ernzerhof) functional and (*b*) the HSE (Heyd-Scuseria-Ernzerhof) functional with a mixing parameter of 0.37. (*c*) The effect of HSE on the position of the valence-band and conduction-band edges with respect to those in generalized gradient approximation. Adapted with permission from Reference 58. Copyright 2009, the American Physical Society.

energy levels have also helped clarify the mechanisms by which defects such as the NV^- center in diamond respond to manipulation (Section 4.4).

The second role is to identify new systems that are suitable for quantum applications. The PL line shape calculations (Section 4.3) allow us to determine whether novel defects will have large DW factors suitable for SPEs. As another example, the ability to accurately calculate defect energy levels (Section 4.2), excited states (Section 4.4), and magnetic properties (Section 4.5) allows one to search for defects that meet the criteria of Reference 8 for qubit applications.

4.1. Formation Energies

The basis for a first-principles study of a given defect for any of the quantum applications in Section 2 is the calculation of the formation energy of the defect in each of the relevant charge states. The formation energy determines the concentration of the defect expected in thermal equilibrium (10). Even in cases in which defects are incorporated under conditions far from equilibrium, such as by implantation, the relative formation energies of different configurations can still shed light on preferential locations in the lattice. Regardless of the incorporation conditions, the information about relative formation energies of different charge states as a function of Fermi level is crucial since it determines the accessible ground-state charge states of the defect, as well

as charge-state transition levels. In general, defects will exhibit a charge and spin configuration suitable for specific qubit or metrology applications only in a specific charge state; for example, the NV center in diamond needs to be in the − charge state to exhibit the level structure in **Figure 1**.

For a general defect X in the charge state q, the formation energy $E_f[X^q]$ is given by (10, 60, 61)

$$E_f[X^q] = E_{tot}[X^q] - E_{tot}[\text{bulk}] - \sum_i n_i \mu_i + qE_F + E_{corr}, \quad 1.$$

where $E_{tot}[X^q]$ is the total energy of a supercell containing the defect in charge state q and $E_{tot}[\text{bulk}]$ is the total energy of the defect-free supercell (a supercell is a volume of the crystal containing many unit cells that is periodically repeated). The chemical potential terms (μ_i) account for the species either added ($n_i > 0$) or removed ($n_i < 0$) from the supercell to create the defect. These terms represent the chemical reservoirs with which atomic species are exchanged, and bounds for these chemical potentials can be set on the basis of the energy of the pure bulk phases of the species or mixed secondary phases.

The term proportional to E_F accounts for the electrons added (for $q < 0$) or removed (for $q > 0$) from the defect supercell. The energy of the reservoir for electron exchange is the electron chemical potential or Fermi level (E_F), which is conventionally referenced to the valence-band maximum (VBM). The final term in Equation 1 is a correction term that accounts for finite-size effects that arise due to the use of the supercell technique and can be due to finite k-point meshes, elastic interactions, electrostatic interactions, etc. Among these, electrostatic interactions are often the most important, and a number of methods have been proposed for quantifying these effects (62–64), as discussed in reviews (10, 65).

We now discuss this methodology by using the example of the V_{Si}-V_C center in 4*H* SiC, which has been reported to be a promising analog to the NV center in diamond (66–68). For this defect, Equation 1 would be written as

$$E_f[(V_{Si}\text{-}V_C)^q] = E_{tot}[(V_{Si}\text{-}V_C)^q] - E_{tot}[\text{bulk}] + \mu_{Si} + \mu_C + q\,E_F + E_{corr}. \quad 2.$$

When referenced to their bulk phases, the chemical potentials μ_{Si} and μ_C can vary between 0 eV (representing the Si- or C-rich limit) and the enthalpy of formation of SiC (representing either the Si- or C-poor limit). For the results presented below, we assume C-rich conditions.

Each charge state q is set by altering the occupation of the defect-related Kohn-Sham states. In this section, we confine our discussion to ground states. As shown in **Figure 3*a***, V_{Si}-V_C gives rise to a_1 and e states within the 4*H* SiC band gap derived from the six dangling bonds of the atoms surrounding the vacancy. In the neutral charge state $(V_{Si}\text{-}V_C)^0$, six electrons are available (one from each dangling bond), leading to the a_1 states being doubly occupied and two of the e states being singly occupied and resulting in an $S = 1$ spin state. In this charge state the defect is therefore analogous to the NV^- center in diamond. Adding another electron to one of the e states stabilizes the $(V_{Si}\text{-}V_C)^-$ charge state, while doubly occupying both of the lower e states gives rise to $(V_{Si}\text{-}V_C)^{-2}$. Removing an electron from an e state yields the $(V_{Si}\text{-}V_C)^+$ charge state.

The +, 0, −, and −2 charge states of $(V_{Si}\text{-}V_C)$ are the ones that can be stabilized within the band gap of 4*H* SiC (**Figure 3*b***). The formation energies of these charge states (as calculated in Reference 67) are shown in **Figure 3*b*** as a function of the Fermi level, which varies from the VBM (set to 0 eV) to the conduction-band minimum (CBM) (at 3.17 eV). Plots such as the one shown in **Figure 3*b*** indicate over what range of Fermi levels a given charge state is stable, which is determined by whichever charge state has the lowest formation energy for a given value of E_F. The slope of each line corresponds to the charge state of the defect. Intersections between these lines represent thermodynamic transition levels (i.e., equilibrium between the two charge states) and are discussed in Section 4.2.

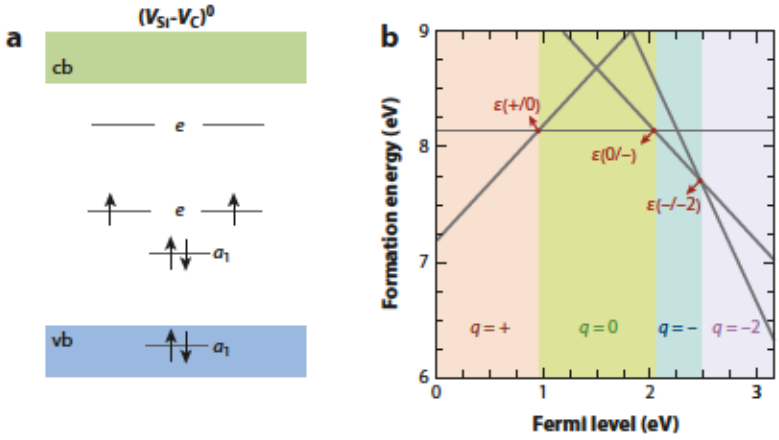

Figure 3

(*a*) Single-particle energy states for $(V_{Si}$-$V_C)^0$ in 4*H* SiC labeled with their C_{3v} irreducible representations. Abbreviations: cb, conduction band; vb, valence band. (*b*) Formation energy versus Fermi level for $(V_{Si}$-$V_C)$ in 4*H* SiC. The charge states that are stable for specific ranges of the Fermi level are labeled, and charge-state transition levels are indicated. Adapted with permission from Reference 67. Copyright 2015, the American Physical Society.

Figure 3*b* shows that, for V_{Si}-V_C to be used as a stable qubit (i.e., for it to have electronic structure analogous to the NV^- center in diamond), the Fermi energy needs to be fixed in between 1 and 2 eV, where the neutral charge state has the lowest energy. This could be achieved either by doping or by electrostatic gating.

4.2. Thermodynamic Transition Levels

On the basis of the knowledge of the formation energies of different charge states q and q', the thermodynamic transition level (referenced to the VBM) is defined as

$$\epsilon(q/q') = \frac{E^f(X^q;\quad E_f = 0) - E^f(X^{q'};\quad E_f = 0)}{q' - q}, \qquad 3.$$

where $E^f(X^q; E_f = 0)$ is the formation energy of defect X in charge state q when the Fermi level is at the VBM. This definition implies that for E_F below $\epsilon(q/q')$, charge state q is stable, while for E_F above $\epsilon(q/q')$, q' is stable. These thermodynamic transition levels are clearly important within the context of quantum information since they define the Fermi-level regions over which specific charge states (and spin configurations) are stable. Furthermore, these levels correspond to the threshold ionization energy required to change the charge state of a defect through exchange of a carrier with a bulk band (corresponding to the ZPL of the transition; see Section 4.3).

We illustrate thermodynamic transition levels for our example of the divacancy in 4*H* SiC. With four stable charge states of this defect, three transition levels occur within the band gap, marked in **Figure 3*b***: $\epsilon(+/0)$, $\epsilon(0/-)$, and $\epsilon(-/-2)$. As an example of estimating threshold ionization energies, if V_{Si}-V_C were stable in the − charge state but the 0 charge state were desired, the defect could be photoionized through excitation of an electron from the defect states to the CBM. This would require an energy of at least 3.17 eV − 2.04 eV = 1.13 eV.

The computational scheme outlined above can be used to enhance the understanding of well-characterized defects such as NV^- in diamond (8) or to computationally search for new defects

in existing materials or defects in novel materials that may be useful for quantum applications. For instance, calculations of transition levels have been performed for a variety of defects, both experimentally detected and theoretically proposed, in various polytypes of SiC (20, 67, 69); additionally, NV^--related defects (70, 71) and split interstitials (72) have been proposed as candidate spin qubits in AlN.

4.3. Optical Properties of Defects

The optical properties of defects play a key role in quantum applications. The most obvious example is in the case of SPEs, which require specific PL properties (such as a large amount of spectral weight in the ZPL) to produce single, indistinguishable photons (6, 25). Applications of defects in quantum computing and metrology also often rely on optical signatures (see Section 2). As mentioned in Section 4.1, light can also be used to ionize a defect, changing its charge state. Finally, the PL line shape (intensity versus emission energy) of a defect can be used as a fingerprint, allowing for identification of the microscopic nature of the defect.

Optical emission at defects can occur via two possible processes: (*a*) an internal transition, where the initial and final states are both defect states and the defect does not change charge state in the process, and (*b*) a capture process, in which the charge state of the defect changes. In case *b*, an electron can be captured from the conduction band, or a hole can be captured from the valence band (corresponding to an electron being emitted to the valence band). The methodology to determine the position of thermodynamic transition levels within the gap is described in Sections 4.1 and 4.2. For case *a*, the excited electronic states of the defect must be treated explicitly; this is discussed in Section 4.4.

Recent advances in first-principles methodologies have generated a powerful toolkit for predicting and studying properties of the optical spectrum, including the position in energy of the PL peak and the line shape of the luminescence.

4.3.1. Configuration coordinate diagrams. In the case of an isolated atom, transitions between states occur at specific energies, resulting in sharp spectral lines. In the case of PL or absorption at defects in a crystal, transitions may be significantly broadened in energy resulting from intrinsic coupling of the electronic structure of the defect with lattice vibrations (both bulk phonons and localized vibrational modes around the defect) and from so-called inhomogeneous broadening caused by differences in the environment around each defect (related to strains or electric fields) (73, 74). Here we consider the effect of the coupling to the lattice; inhomogeneous broadening can be evaluated using first-principles calculations, but we do not discuss it further in this review.

A useful conceptual and computational approach to describing this coupling and its effect on optical transitions is so-called configuration coordinate (CC) diagrams, as shown in **Figure 4*a*,*c***. The vertical axis is the energy of the transition, and the horizontal axis is some generalized coordinate that is a one-dimensional (1D) parameterization of a collective atomic displacement. For a given state of the defect, we expect a roughly parabolic potential energy surface with a minimum at the ground-state atomic configuration of the defect.

In **Figure 4*a***, we show a CC diagram (calculated using DFT with the HSE functional) for an electron capture process at a positively charged defect complex in GaN consisting of a gallium vacancy with a nearest-neighbor nitrogen atom replaced by an oxygen atom, plus two hydrogen atoms. The complex is denoted V_{Ga}-O_N-2H and is described in detail in References 75 and 77; it has only two stable charge states, namely + and 0. The generalized coordinate Q is taken to be a linear interpolation between the atomic positions in the equilibrium structures of the + and 0 charge states of the defect (more on this in Section 4.3.2). The upper curve corresponds to the

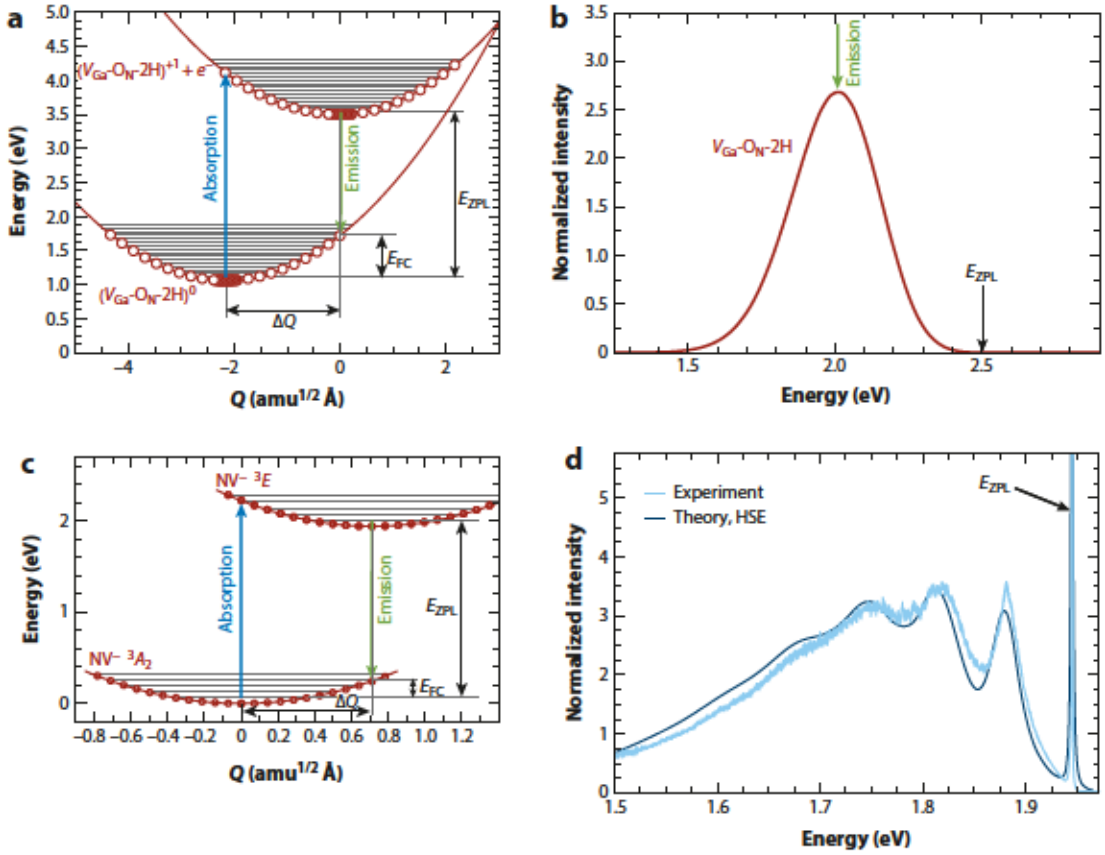

Figure 4

(*a*) Calculated configuration coordinate (CC) diagram for electron capture process at a $(V_{Ga}\text{-}O_N\text{-}2H)^+$ defect complex in GaN. (*b*) Calculated photoluminescence line shape for this process. Panel *b* adapted from Reference 75 and reproduced with permission. Copyright, John Wiley & Sons. (*c*) Calculated CC diagram for the triplet-triplet transition at the nitrogen vacancy (NV^-) in diamond. (*d*) Calculated and experimental photoluminescence line shapes for this transition. Panels *c* and *d* adapted from Reference 76. Abbreviations: FC, Frank-Condon; HSE, Heyd-Scuseria-Ernzerhof; ZPL, zero-phonon line.

defect in a + charge state plus an electron in the GaN conduction band, while the lower curve corresponds to the neutral charge state of the defect. The minima of the curves are offset in Q as a result of electron-phonon coupling (EPC); the strength of the EPC can be quantified by the so-called Huang-Rhys (HR) factor S (78), which is essentially the average number of phonons emitted during an optical transition.

Figure 4*c* is a calculated CC diagram for the triplet-triplet transition of the NV^- center in diamond (from Reference 76). Here, the upper curve corresponds to the ^3E excited state of the defect, and the lower curve to the $^3A_2$ ground state. Q is again chosen to be a linear interpolation of the atomic positions between the equilibrium structures of the ground and excited states. The transition in **Figure 4*c*** has much weaker EPC than does the case of **Figure 4*a***.

In **Figure 4*a*,*c***, the horizontal lines in the energy-versus-Q curves denote vibrational energy levels. The emission arrows correspond to a possible emission event from the ground vibrational state of the excited electronic state. Within the frequently used Franck-Condon approximation, the electronic transition of the radiative process is assumed to occur without atomic motion (79),

so it is vertical on the CC diagram. The final state for this transition is a highly excited vibrational state of the ground electronic state; the system will rapidly transition to the ground vibronic state through the emission of phonons, losing energy equal to the so-called Frank-Condon relaxation energy, E_{FC}. The ZPL energy, corresponding to the transition in which no phonons are emitted, is also indicated in **Figure 4*a*,*c***. It constitutes the highest-energy transition (at low temperature, at which only the lowest vibrational state of the excited electronic state is occupied).

For a carrier capture process such as the one in **Figure 4*a***, E_{ZPL} can be obtained by calculating the charge-state transition levels, using the methodology of Section 4.2. For example, the ZPL energy for electron capture at the $(V_{Si}\text{-}V_C)^0$ defect is the energy difference between the $\varepsilon(0/-)$ level and the conduction band (see **Figure 3*b***). The energies of the transitions at other Q values can be similarly obtained by carrying out calculations for each of the two charge states for the corresponding atomic configurations. For an internal transition at a defect, such as the ^3E-to-$^3A_2$ transition of the NV^- center in diamond (**Figure 4*a***), the energy of the excited state must be calculated using a different methodology, as discussed in Section 4.4.

4.3.2. Photoluminescence line shapes. In general, the wave functions describing the defect system are functions of all electronic ($\{x\}$) and ionic ($\{Q\}$) degrees of freedom; by using the Born-Oppenheimer approximation (44), they can be written in the form $\Psi(\{x\};\{Q\})\chi(\{Q\})$, where $\Psi(\{x\};\{Q\})$ is the electronic wave function (which depends parametrically on $\{Q\}$), and $\chi(\{Q\})$ is the ionic wave function. Optical transitions occur because of coupling to an electric field, described by the transition dipole matrix element between the ground (g) and excited (e) states, $\boldsymbol{\mu}_{eg}$; within the Frank-Condon approximation, where it is assumed that $\boldsymbol{\mu}_{eg}$ does not depend on Q (79), the absolute luminescence intensity (the number of photons per unit time per unit energy for a given photon energy $\hbar\omega$) is given by (in SI units) (74)

$$I(\hbar\omega, T) = \frac{n_r\omega^3}{3\varepsilon_0\pi c^3\hbar}\left|\boldsymbol{\mu}_{eg}\right|^2 \sum_{n,m} w_n(T)|\langle\chi_{gm}|\chi_{en}\rangle|^2\delta(E_{ZPL} - E_{gm} + E_{en} - \hbar\omega), \qquad 4.$$

where n_r is the index of refraction, c is the speed of light, χ_{em} (χ_{gn}) is the vibrational wave function for the m (n) vibrational state of the excited (ground) electronic state, E_{gm} (E_{en}) is the energy of the state χ_{gm} (χ_{en}), E_{ZPL} is the energy of the ZPL, and $w_n(T)$ is the thermal occupation of the excited state. In Equation 4 we have neglected the temperature dependence of the E_{ZPL}, so any temperature dependence enters purely through the thermal occupation of the excited vibrational state. Experiments usually report a normalized intensity, so for the calculation of PL line shapes, we can focus on the ω dependence of Equation 4.

The rate of radiative transitions, which is important for determining excited-state lifetimes and internal quantum efficiencies of emitters, can be obtained by integrating the absolute PL intensity (Equation 4) over the energy range of the line shape and therefore requires calculation of the transition dipole matrix element and the average energy of the vertical transition. Estimates of the ^3E excited-state ($m_s = 0$ spin sublevel) lifetimes from calculated radiative transition rates for the NV^- center in diamond [20 ns (80), 13.1 ns (81), and 10 ns (82)] are within the experimental range of 10–25 ns (see Reference 9 for a summary of experiments). Significantly, calculation of the excited-state lifetimes of the $m_s = \pm 1$ sublevels of ^3E is complicated by the fact that nonradiative decay can occur from these states via the ISC.

The challenge for calculations of Equation 4 is the overlap of vibrational wave functions, $\langle\chi_{gm}|\chi_{en}\rangle$. In principle this requires summing over all vibrational modes of a crystal with a defect in both the excited and ground states and thus leads to a highly multidimensional integral. The treatment of the overlap depends on the strength of the EPC (83). In the case of capture processes or intradefect transitions with strong EPC, $S \gg 1$ (for example, the capture process in **Figure 4*a***

has $S = 15$), it has often been assumed that a 1D approximation to the full vibrational problem is sufficient to determine the vibrational overlap and therefore the line shape (74, 79, 84). Within this approximation, a single effective mode (not necessarily a normal mode of the excited or ground state) is chosen to describe the vibrational coupling. Alkauskas et al. (85) used hybrid-functional calculations to demonstrate the accuracy of the 1D approximation in the $S \gg 1$ case by choosing the vibrational mode to be a linear interpolation between the equilibrium structures of the excited and ground states. Accurate line shapes were obtained for deep defects with large S in GaN and ZnO. It was observed that the frequency of this effective mode is significantly smaller than that of the longitudinal optical mode of the materials studied (75, 85).

This effective mode is the one corresponding to the coordinate Q plotted in **Figure 4*a*,*c*** and used to calculate the line shape in **Figure 4*b*** (75). The PL line shape in **Figure 4*b*** is approximately Gaussian, with most of the spectral weight in the phonon side band. The PL peak occurs at the energy of the classical vertical transition (which would be obtained by neglecting the fact that the initial vibrational state is described by a wave function with finite overlap with multiple vibrational levels in the ground state) denoted by the emission arrow in **Figure 4*a*,*b***, and the absorption peak would occur at the energy of the absorption arrow in **Figure 4*a***. Within the 1D approximation, and assuming an equal vibrational frequency in the excited and ground states, the HR factor is $S_{1D} = E_{FC}/\hbar\omega_0$, where ω_0 is the vibrational frequency of the effective mode.

Also under the assumption of equal vibrational frequencies in the excited and ground states (but irrespective of whether or not the 1D approximation was made), and neglecting the $\sim\omega^3$ prefactor in Equation 4, the relative spectral weight in the ZPL is given by $w_{ZPL} = e^{-S}$ (the DW factor mentioned in Section 2.2) (16, 84). This form of w_{ZPL} clearly demonstrates that the ZPL has very little weight in the case of strong EPC ($S \gg 1$).

Another limiting case occurs when S is small enough to ensure that the weight of the PL spectrum is in the ZPL (a large DW factor) and that the intensity of the phonon side band is very weak; this occurs for capture processes or intradefect transitions with small EPC. From a computational perspective, the most difficult cases are the ones with an intermediate EPC strength. The triplet transition of the NV^- center in diamond is a good example, with an experimentally determined value of the HR factor $S = 3.73$ (28). As evident from **Figure 4*d***, in this case there is significantly more spectral weight in the ZPL and more structure in the phonon side band than in the $S = 15$ case of **Figure 4*b***. The classical vertical emission no longer corresponds to a clear peak in the spectrum. In this case, the 1D approximation is no longer adequate for predicting the PL line shape (74, 83), and an approach that explicitly treats vibrational modes with different frequencies is required.

Under the assumption that the vibrational modes are identical in the excited and ground states, the generating-function approach (79, 86) can be used. This method involves summing so-called partial HR factors, S_k, for each of the relevant phonon modes to obtain the spectral function of EPC, $S(\hbar\omega) = \sum_k S_k \delta(\hbar\omega - \hbar\omega_k)$, and total HR factor $S = \sum_k S_k$. On the basis of Equation 4, the (zero-temperature) normalized luminescence can be written as (79, 86)

$$L(E_{ZPL} - \hbar\omega) = C\omega^3 \int_{-\infty}^{\infty} \left(e^{S(t)-S(0)}\right) e^{i\omega t - \gamma|t|} \mathrm{d}t, \qquad 5.$$

where $S(t) = \int_0^\infty S(\hbar\omega) e^{-i\omega t} \mathrm{d}(\hbar\omega)$ is the Fourier transform of $S(\hbar\omega)$ and γ is a parameter that represents the broadening of the ZPL.

Alkauskas et al. (76) used this approach to determine the PL line shape for the ^3E-to-$^3A_2$ transition of the NV^- center in diamond. As shown in **Figure 4*d***, excellent agreement was obtained with the experimental line shape, as well as the HR factor (calculated $S = 3.67$) and DW factor [calculated $w_{ZPL} = 3.8\%$ versus experimental $w_{ZPL} = 3.2\%$ (28)]. We note that the assumption

that the vibronic modes are identical in the excited and ground states is not strictly fulfilled in the case of NV^- in diamond (87); this may be one reason why the calculated line shape (**Figure 4*d***) exhibits minor deviations from the experimental spectrum.

This study of the NV^- center demonstrated that an accurate treatment of vibrational modes (beyond the 1D approximation) is essential to quantitatively reproduce the PL line shape in the case of intermediate EPC strength: Localized vibrational modes around the defect, quasi-localized defect-induced vibrational resonances, as well as long-range acoustic modes, needed to be included (76). In general, defects with intermediate EPC will require the inclusion of contributions from various types of vibrational modes.

4.4. Excited States

When intradefect transitions are used for quantum applications, a quantitative understanding of excited electronic states is crucial. However, Kohn-Sham DFT is inherently a ground-state theory, and hence excited states require particular attention. In this section, we briefly summarize the approaches to treating excited states, as they apply to the calculation of properties discussed in Sections 4.2 and 4.3.

4.4.1. Constrained density functional theory. As discussed in Section 3, two of DFT's main advantages over higher-level techniques are its relatively low computational cost, allowing for calculations of large and complex systems, and the ability to efficiently perform atomic relaxations. These benefits are especially crucial for defect calculations since large supercells or clusters are required to model an isolated defect and large numbers of calculations are typically required to characterize the atomic and electronic structure of the defect. Therefore, there is a significant incentive for devising DFT-based techniques that can provide a qualitative and even quantitative understanding of properties connected to excited states.

The central issue is that the KS eigenvalues from DFT do not correspond to quasi-particle addition and removal energies. This is a result of the self-interaction errors inherent in local and semilocal DFT functionals (48, 88). Much research effort (see, e.g., References 89 and 90) has been aimed at developing approximate functionals that would cure this shortcoming. It has been demonstrated for several systems that self-interaction errors are greatly reduced in hybrid functionals, specifically for the HSE functional (91, 92).

Excited states can be approximately treated within DFT by using the constrained DFT (CDFT) approach. This method is quite general (see Reference 93 for a review) and involves including an additional Lagrange parameter when minimizing the density functional, resulting in an additional potential in the Kohn-Sham equations (94, 95). In the case of excited states at defects, the constraining potential is chosen such that the ground state of the defect system in the presence of the potential mimics the excited state of interest. For example, the symmetry (e.g., angular momentum or spin) of the wave functions can be constrained (96), or the occupation of a given orbital can be specified. For the example of the single-particle states of the NV^- in diamond (**Figure 1*b***) or $(V_{Si}\text{-}V_C)^0$ in SiC (**Figure 3*a***), an approximation of the ^3E electronic excited state may be created by constraining the a_1 orbital to be half filled so that an electron is forced to occupy the empty spin channel of the e states.

CDFT calculations have been applied to the excited states of the NV^- center in diamond (**Figure 1*c***) (8, 76, 80, 97–100). Using local/semilocal functionals, Goss et al. (80) and Delaney et al. (99) determined the energetic ordering of these excited states, which was found to be in agreement with more advanced calculations (References 99 and 101, discussed in Sections 4.4.2 and 4.4.4). When CDFT is used in conjunction with the HSE functional, calculations give values

of E_{ZPL} for NV^- [2.02 (8), 2.035 (76), and 1.955 (100)], in good agreement with experiment [1.945 eV (102)]. Similar accuracy (~0.1 eV) was demonstrated for the ZPL of the divacancy in various polytypes of SiC (67, 103).

Overall, CDFT calculations have provided crucial insights into excited-state properties of quantum defects, particularly when combined with hybrid functionals. An important limitation, however, is that CDFT is in principle applicable only to situations in which the many-body electronic state reduces to a single Slater determinant of single-particle orbitals (104). In the following sections, we discuss several higher-level techniques that address the shortcomings of DFT for excited states and multideterminant states.

4.4.2. Many-body perturbation theory. Many-body perturbation theory (MBPT) methods based on the *GW* approximation apply a quasi-particle correction to the KS eigenvalues of a traditional DFT or hybrid functional calculation (105); the resulting energy states therefore more rigorously correspond to the single-particle excitation energies (within the accuracy of the approximations). Significant advances have been made in *GW* calculations of charge-state transition levels (106). The interaction between an excited electron and resulting hole (in the case of a neutral excitation) can be accounted for by solving the Bethe-Salpeter (BSE) equation (105).

GW and *GW*+BSE techniques, however, have significant limitations. Because of the much larger computational cost of these techniques, convergence with respect to numerical parameters may be difficult for the large supercell sizes necessary for defect calculations. Also, within MBPT it is generally not possible to calculate forces on atoms in solids in a computationally tractable way, causing the final result to depend on the accuracy of the atomic structure of the defect calculated with DFT.

Optical transitions and absorption spectra for color centers, including the F centers in CaF_2 (82), LiCl (107, 108), LiF (109), and MgO (110), were studied with *GW* and/or *GW*+BSE. Ma et al. (101) used *GW*+BSE to calculate the excited states of the NV^- center in diamond, supporting CDFT predictions of excited-state orderings (80, 99). Relaxed structures in the excited state in Reference 101 were obtained with CDFT. The results for absorption, emission, and ZPL energies for the triplet states agree with experiment about as well as those based on CDFT-HSE discussed in Section 4.4.1. Bockstedte et al. (111) used *GW*+BSE calculations of carbon vacancies in SiC to interpret photo–electron paramagnetic resonance (EPR) measurements. Attaccalite et al. (112) performed MBPT calculations on defects in BN and their coupling to bulk excitons. Finally, Szász (69) combined hybrid functional and *GW*+BSE calculations on the carbon-antisite vacancy defect in 4*H* SiC, identifying it as a possible spin qubit.

4.4.3. Time-dependent density functional theory. Time-dependent density functional theory (TDDFT) is a generalization of Hohenberg-Kohn-Sham DFT to time-dependent potentials (113), allowing for the application of density-based techniques to the calculation of excited-state spectra. Although TDDFT has enjoyed considerable success for finite systems such as molecules and small clusters, its application to solids has proved challenging (see Reference 114 for a review). As with standard DFT, hybrid functionals combined with TDDFT improve the accuracy of optical spectra for solids relative to TDDFT with local and semilocal functionals (115). Only a few TDDFT studies of defects have been performed, using clusters to approximate the infinite solid. Gali (21) used TDDFT (on clusters) to compare vertical excitation energies for NV^- in diamond, finding that the CDFT-HSE value (2.21 eV) was in very good agreement with the TDDFT result [in which the PBE0 functional (116) was used] and with experiment (2.18 eV from Reference 102), while the *GW*+BSE value was slightly larger (2.32 eV). Gali also performed calculations for the neutral divacancy in SiC (21). Zyubin et al. (117) performed TDDFT

calculations on the NV^- center and compared their results to configuration interaction (CI) calculations (see below).

4.4.4. Configuration interaction. The CI method is a quantum chemistry technique in which the many-body wave function is written as a linear combination of Slater determinants of single-particle wave functions with coefficients determined using the variational approach. In principle, "full" CI (including all possible Slater determinants of a complete orbital basis) gives the exact solution to the many-body Schrödinger equation and allows for the calculation of intrinsically multideterminant states. In practice, the technique is severely limited by its computational complexity. Even when significant approximations are made (by limiting the number of Slater determinants and/or the size of the orbital basis), CI is computationally tractable only for small systems such as molecules and simple solids (118). Because of these computational limitations, few CI studies have been performed for defects. The calculations of Delaney et al. (99) and Zyubin et al. (117) on small diamond clusters helped clarify the ordering of the singlet excited states of the NV^- center.

4.5. Magnetic Properties

In addition to the electronic and optical properties of defects, magnetic properties are very important for understanding and realizing the potential of defects for quantum computing and metrology. In this section we discuss first-principles methodologies and relevant calculations for hyperfine (hf) coupling, ZFS, and the g tensor for quantum defects. These properties have been chosen as examples to demonstrate the capabilities and accuracy of first-principles calculations; other relevant magnetic properties include the strength of spin-orbit interaction and magnetic quadrupole spectra.

4.5.1. Hyperfine coupling. Hyperfine coupling is the interaction between the electron spin and nuclear spin. It causes splittings in EPR/electron spin resonance (ESR), ODMR, or electron-nuclear double-resonance (ENDOR) spectral lines. Quantitative first-principles calculations of hf tensors are a powerful tool for identifying the chemical nature and structure of paramagnetic defects detected in any of these techniques. In addition, the hf interaction could be used to couple electron spins at defects to nearby nuclear spins (as discussed in Section 2.1) and even to map electron spins to nuclear spins, as experimentally demonstrated in References 119 and 120 and described theoretically in Reference 121. An illustration of a calculated electron spin density is shown in **Figure 5** for a divacancy defect in *6H* SiC.

The hf interaction, parameterized by the hf tensor, has two parts: the isotropic Fermi contact term and the anisotropic dipolar part. Both of these parts require calculation of the electron spin density at or around the atomic nuclei. Techniques to perform the calculations of hf tensors have been developed for DFT calculations in which atomic cores are treated with pseudopotentials (122, 123) or with PAWs (124) and for local/semilocal exchange-correlation functionals as well as hybrid functionals (125).

A number of calculations of hf tensors have been published for defects for quantum applications. For example, for the NV^- center in diamond, DFT calculations by Gali and coworkers were critical in clarifying the sign of the hf parameters for ^{14}N and ^{15}N (97, 126, 127). LDA calculations of the ^{15}N axial and nonaxial hf parameters for the NV^0 center (127) (axial: −39.0 MHz; nonaxial: −23.4 MHz) compared favorably with experimental values (128) of −35.7 MHz and −23.8 MHz. PBE calculations for NV^- (axial: 2.3 MHz; nonaxial: 2.7 MHz) also compared well with experiment [3.01 MHz (119) and 3.03 MHz (128)]. These examples demonstrate the accuracy and utility of first-principles calculations of hf tensors for defect-state and/or charge-state identification.

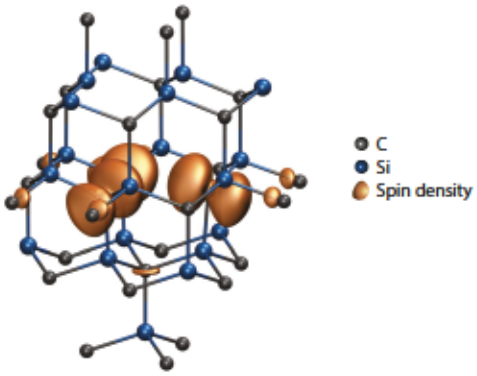

Figure 5

DFT spin density of a neutral divacancy in *6H* SiC for calculation of hyperfine coupling. Adapted with permission from Reference 121. Copyright, the American Physical Society. Figure courtesy of A. Gali and V. Ivady.

parameters have also been calculated for various defects of interest in SiC to aid in identification (see Reference 129 and references therein, Reference 130, and Reference 131). Szállás et al. (72) also performed calculations of hf parameters for the split N interstitial in AlN.

4.5.2. Zero-field splitting. In an atom, spin sublevels that correspond to different projections of the spin are energy degenerate. This is not necessarily the case in a reduced-symmetry environment such as a molecule or a defect in a solid. For example, as discussed in Section 2.1, the NV^- in diamond has a 2.88-GHz splitting between the $m_s = 0$ and $m_s = \pm 1$ levels (**Figure 1*c***). This so-called ZFS is caused by magnetic dipole-dipole and spin-orbit interactions.

The fine structure caused by ZFS is sensitive to the symmetry of the defect and to the spatial extent of the defect wave function (74); measurements of the ZFS by ESR or ODMR therefore provide information about the defect structure. As discussed in Section 2.3, the magnitude of the ZFS between $m_s = 0$ and $m_s = \pm 1$ levels in triplet states (ground or excited) of NV^- in diamond can be used as a probe for various external perturbations such as temperature, strain, and electric field (132).

Relative to hf parameters and *g* tensors, fewer calculations of ZFS have been reported. ZFS have been calculated in molecules with DFT and quantum chemistry techniques (133). For defects with light atoms such as C and Si, the dipole-dipole part is expected to dominate in the ZFS. Methodologies to calculate dipole-dipole interactions with DFT for defects in solids have been developed (134, 135), and Ivady et al. (136) applied such methodologies to determine the pressure and temperature dependence of the ZFS for NV^- in diamond. A zero-pressure value of $D = 2.84$ GHz (extracted from figure 3 of Reference 136) and a slope with hydrostatic pressure (over a range from 0 to 50 GPa) of 10.30 MHz/GPa were obtained, in good agreement with the value of 14.58 MHz/GPa experimentally determined by Doherty et al. (137). ZFS calculations have also been used to help identify the NV^- center in the various polytypes of SiC via EPR (138).

4.5.3. *g* tensor. Under the application of a magnetic field, the Zeeman effect, in which the spin sublevels split, occurs. The spin Hamiltonian contains terms for the nuclear and electron Zeeman effects. The electronic *g* tensor for paramagnetic defects is probed directly with ESR and ODMR, and first-principles predictions provide an important tool for defect identification. In addition, knowledge of the *g* tensor is essential for magnetic-field nano-sensing applications (132).

First-principles calculations (using a variety of computational methods) of g tensors for molecules are widespread (133); a DFT implementation was first developed by Schreckenbach & Ziegler (139). Pickard & Mauri (140) subsequently developed a methodology for calculations on extended systems (including defects in supercells). von Bardeleben et al. (138) calculated g tensors for the NV^- center in the various polytypes of SiC and compared these calculations to EPR results; PBE calculations gave g-tensor elements of 2.0034–2.0036 (depending on the polytype) for the axial component and 2.0029 for the nonaxial component, compared to experimental values of 2.004 for the axial component and 2.003 for the nonaxial component (138).

5. SUMMARY AND OUTLOOK

Point defects in semiconductors and insulators offer an exciting platform for technologies based on the unique aspects of quantum mechanics. They show promise as spin qubits and quantum memories for computing, SPEs for nonclassical communication and cryptography as well as optical quantum computing, and sensors for nanoscale metrology. To realize this potential, a quantitative understanding of the electronic, atomic, optical, and magnetic properties of defects is required. We show above that first-principles calculations are playing a crucial role in understanding the properties of known defects and in identifying and characterizing novel defects. While great advances have been made in computational power and methodology, there are still open questions and many active areas of research:

1. As is evident from Section 4.4, there is still much work to be done with regard to the treatment of excited states. The application of the discussed beyond-DFT techniques is not yet routine as a result of significant computational and methodological limitations. Even for the best-studied example, the NV^- center in diamond, difficulties persist in determining accurate energies for the intrinsically multideterminant excited states. Progress could involve improving DFT-based schemes such as CDFT with hybrid functionals, making higher-level methods more computationally tractable, or some combination of the two.
2. First-principles methodologies for intradefect nonradiative transitions need to be developed, a need that is illustrated by the fact that, even for the NV^- center in diamond, the nature of the nonradiative transitions is not settled. The approach would build on the recently developed treatment of capture processes (141).
3. Further improvements in the computational treatment of the vibrational structure of defects are desirable to enable more efficient calculations of, e.g., luminescence line shapes (see Section 4.3.2).
4. DFT calculations offer high accuracy (particularly with hybrid functionals) at an acceptable computational cost. However, even hybrid functionals lack long-range electron correlations, which manifest, for instance, in van der Waals interactions; efforts to include the latter in DFT calculations are well under way (142). More generally, correlations can be captured using orbital-dependent functionals, such as random-phase approximation (RPA) functionals (143). High computational cost is an obstacle, and there have hence been very few applications to defects (144). Still, the application of RPA and related functionals should be a fruitful area of research in the coming years.
5. The first-principles methodology described in this review holds great promise for systematic surveys of potential defects in a range of materials. Automating such searches would be desirable but requires great care and caution in choosing descriptors, particularly in an area in which physical understanding is still incomplete. Appropriate guided-search strategies still need to be developed.

Overall, we are confident that first-principles methods will continue to play an increasingly important role in understanding and predicting point defects for quantum technologies.

DISCLOSURE STATEMENT

The authors are not aware of any affiliations, memberships, funding, or financial holdings that might be perceived as affecting the objectivity of this review.

ACKNOWLEDGMENTS

We are grateful to M. Doherty for valuable discussions and for a critical reading of the manuscript and to V. Ivady and A. Gali for providing us with **Figure 5**. C.G.V.d.W. was supported by Basic Energy Sciences, Office of Science, US Department of Energy, under award DE-SC0010689. A.A. was supported by the Research Council of Lithuania (grant M-ERA.NET-1/2015) and by the National Science Foundation IMI program (grant DMR08-43934). J.L.L. was supported by the Office of Naval Research through the Naval Research Laboratory's Basic Research Program. A.J. was supported by NSF Early Career award DMR-1652994.

LITERATURE CITED

1. Feynman RP. 1982. Simulating physics with computers. *Int. J. Theor. Phys.* 21:467–88
2. Monroe C. 2002. Quantum information processing with atoms and photons. *Nature* 416:238–46
3. Lucero E, Hofheinz M, Ansmann M, Bialczak RC, Katz N, et al. 2008. High-fidelity gates in a single Josephson qubit. *Phys. Rev. Lett.* 100:247001
4. Michler P. 2017. *Quantum Dots for Quantum Information Technologies*. Cham, Switz.: Springer
5. Pla JJ, Tan KY, Dehollain JP, Lim WH, Morton JJL, et al. 2012. A single-atom electron spin qubit in silicon. *Nature* 489:541–45
6. Aharonovich I, Castelletto S, Simpson DA, Su CH, Greentree AD, Prawer S. 2011. Diamond-based single-photon emitters. *Rep. Prog. Phys.* 74:076501
7. Schirhagl R, Chang K, Loretz M, Degen CL. 2014. Nitrogen-vacancy centers in diamond: nanoscale sensors for physics and biology. *Annu. Rev. Phys. Chem.* 65:83–105
8. Weber JR, Koehl WF, Varley JB, Janotti A, Buckley BB, et al. 2010. Quantum computing with defects. *PNAS* 107:8513–18
9. Doherty MW, Manson NB, Delaney P, Jelezko F, Wrachtrup J, Hollenberg LC. 2013. The nitrogen-vacancy colour centre in diamond. *Phys. Rep.* 528:1–45
10. Freysoldt C, Grabowski B, Hickel T, Neugebauer J, Kresse G, et al. 2014. First-principles calculations for point defects in solids. *Rev. Mod. Phys.* 86:253–305
11. Rieffel E, Polak W. 2011. *Quantum Computing: A Gentle Introduction*. Cambridge, MA: MIT Press
12. Ladd T, Jelezko F, Laflamme R, Nakamura Y, Monroe C, O'Brien J. 2010. Quantum computers. *Nature* 464:45–53
13. Kane BE. 1998. A silicon-based nuclear spin quantum computer. *Nature* 393:133–37
14. Zwanenburg FA, Dzurak AS, Morello A, Simmons MY, Hollenberg LCL, et al. 2013. Silicon quantum electronics. *Rev. Mod. Phys.* 85:961–1019
15. Salfi J, Mol J, Rahman R, Klimeck G, Simmons M, et al. 2016. Quantum simulation of the Hubbard model with dopant atoms in silicon. *Nat. Commun.* 7:11342
16. Davies G. 1974. Vibronic spectra in diamond. *J. Phys. C Solid State* 7:3797
17. Gruber A, Dräbenstedt A, Tietz C, Fleury L, Wrachtrup J, Von Borczyskowski C. 1997. Scanning confocal optical microscopy and magnetic resonance on single defect centers. *Science* 276:2012–14
18. Acosta VM, Jarmola A, Bauch E, Budker D. 2010. Optical properties of the nitrogen-vacancy singlet levels in diamond. *Phys. Rev. B* 82:201202

19. Goldman ML, Doherty MW, Sipahigil A, Yao NY, Bennett SD, et al. 2015. State-selective intersystem crossing in nitrogen-vacancy centers. *Phys. Rev. B* 91:165201
20. Weber J, Koehl W, Varley J, Janotti A, Buckley B, et al. 2011. Defects in SiC for quantum computing. *J. Appl. Phys.* 109:102417
21. Gali A. 2011. Time-dependent density functional study on the excitation spectrum of point defects in semiconductors. *Phys. Status Solid. B* 248:1337–46
22. Christle DJ, Falk AL, Andrich P, Klimov PV, Hassan JU, et al. 2015. Isolated electron spins in silicon carbide with millisecond coherence times. *Nat. Mater.* 14:160–63
23. Falk AL, Buckley BB, Calusine G, Koehl WF, Dobrovitski VV, et al. 2013. Polytype control of spin qubits in silicon carbide. *Nat. Commun.* 4:1819
24. O'Brien JL, Furusawa A, Vuckovic J. 2009. Photonic quantum technologies. *Nat. Photonincs* 3:687–95
25. Aharonovich I, Englund D, Toth M. 2016. Solid-state single-photon emitters. *Nat. Photonics* 10:631–41
26. Scarani V, Bechmann-Pasquinucci H, Cerf NJ, Dušek M, Lütkenhaus N, Peev M. 2009. The security of practical quantum key distribution. *Rev. Mod. Phys.* 81:1301–50
27. Beveratos A, Brouri R, Gacoin T, Villing A, Poizat JP, Grangier P. 2002. Single photon quantum cryptography. *Phys. Rev. Lett.* 89:187901
28. Davies G. 1981. The Jahn-Teller effect and vibronic coupling at deep levels in diamond. *Rep. Prog. Phys.* 44:787
29. Dietrich A, Jahnke KD, Binder JM, Teraji T, Isoya J, et al. 2014. Isotopically varying spectral features of silicon-vacancy in diamond. *New J. Phys.* 16:113019
30. Sipahigil A, Jahnke KD, Rogers LJ, Teraji T, Isoya J, et al. 2014. Indistinguishable photons from separated silicon-vacancy centers in diamond. *Phys. Rev. Lett.* 113:113602
31. Kolesov R, Xia K, Reuter R, Stöhr R, Zappe A, et al. 2012. Optical detection of a single rare-earth ion in a crystal. *Nat. Commun.* 3:1029
32. Castelletto S, Johnson BC, Ivady V, Stavrias N, Umeda T, et al. 2014. A silicon carbide room-temperature single-photon source. *Nat. Mater.* 13:151–56
33. Lohrmann A, Johnson BC, McCallum JC, Castelletto S. 2017. A review on single photon sources in silicon carbide. *Rep. Prog. Phys.* 80:034502
34. Pingault B, Becker JN, Schulte CHH, Arend C, Hepp C, et al. 2014. All-optical formation of coherent dark states of silicon-vacancy spins in diamond. *Phys. Rev. Lett.* 113:263601
35. McCumber DE, Sturge MD. 1963. Linewidth and temperature shift of the R lines in ruby. *J. Appl. Phys.* 34:1682–84
36. Sholes RR, Small JG. 1980. Fluorescent decay thermometer with biological applications. *Rev. Sci. Instrum.* 51:882–84
37. Forman RA, Piermarini GJ, Barnett JD, Block S. 1972. Pressure measurement made by the utilization of ruby sharp-line luminescence. *Science* 176:284–85
38. Acosta VM, Bauch E, Ledbetter MP, Waxman A, Bouchard LS, Budker D. 2010. Temperature dependence of the nitrogen-vacancy magnetic resonance in diamond. *Phys. Rev. Lett.* 104:070801
39. Degen CL. 2008. Scanning magnetic field microscope with a diamond single-spin sensor. *Appl. Phys. Lett.* 92:243111
40. Grinolds MS, Hong S, Maletinsky P, Luan L, Lukin MD, et al. 2013. Nanoscale magnetic imaging of a single electron spin under ambient conditions. *Nat. Phys.* 9:215–19
41. Toyli DM, Christle DJ, Alkauskas A, Buckley BB, Van de Walle CG, Awschalom DD. 2012. Measurement and control of single nitrogen-vacancy center spins above 600 K. *Phys. Rev. X* 2:031001
42. Simin D, Fuchs F, Kraus H, Sperlich A, Baranov PG, et al. 2015. High-precision angle-resolved magnetometry with uniaxial quantum centers in silicon carbide. *Phys. Rev. Appl.* 4:014009
43. Martin RM. 2004. *Electronic Structure: Basic Theory and Practical Methods*. Cambridge, UK: Cambridge Univ. Press
44. Born M, Oppenheimer R. 1927. Zur Quantentheorie der Molekeln. *Ann. Phys.* 389:457–84
45. Szabó A, Ostlund N. 1996. *Modern Quantum Chemistry: Introduction to Advanced Electronic Structure Theory*. Mineola, NY: Dover
46. Hohenberg P, Kohn W. 1964. Inhomogeneous electron gas. *Phys. Rev. B* 136:864–71

47. Kohn W, Sham LJ. 1965. Self-consistent equations including exchange and correlation effects. *Phys. Rev. A* 140:1133–38
48. Perdew JP, Zunger A. 1981. Self-interaction correction to density-functional approximations for many-electron systems. *Phys. Rev. B* 23:5048–79
49. Ceperley DM, Alder BJ. 1980. Ground state of the electron gas by a stochastic method. *Phys. Rev. Lett.* 45:566–69
50. Perdew JP, Burke K, Ernzerhof M. 1996. Generalized gradient approximation made simple. *Phys. Rev. Lett.* 77:3865–68
51. Sham LJ, Schlüter M. 1983. Density-functional theory of the energy gap. *Phys. Rev. Lett.* 51:1888–91
52. Godby RW, Schlüter M, Sham LJ. 1986. Accurate exchange-correlation potential for silicon and its discontinuity on addition of an electron. *Phys. Rev. Lett.* 56:2415–18
53. Perdew JP, Parr RG, Levy M, Balduz JL. 1982. Density-functional theory for fractional particle number: derivative discontinuities of the energy. *Phys. Rev. Lett.* 49:1691–94
54. Mori-Sánchez P, Cohen AJ, Yang W. 2006. Many-electron self-interaction error in approximate density functionals. *J. Chem. Phys.* 125:201102
55. Becke AD. 1993. A new mixing of Hartree-Fock and local density-functional theories. *J. Chem. Phys.* 98:1372–77
56. Perdew JP, Ernzerhof M, Burke K. 1996. Rationale for mixing exact exchange with density functional approximations. *J. Chem. Phys.* 105:9982–85
57. Heyd J, Scuseria GE, Ernzerhof M. 2003. Hybrid functionals based on a screened Coulomb potential. *J. Chem. Phys.* 118:8207–15
58. Lyons JL, Janotti A, Van de Walle CG. 2009. Role of Si and Ge as impurities in ZnO. *Phys. Rev. B* 80:205113
59. Alkauskas A, Broqvist P, Pasquarello A. 2011. Defect levels through hybrid density functionals: insights and applications. *Phys. Status Solid. B* 248:775–89
60. Zhang SB, Northrup JE. 1991. Chemical potential dependence of defect formation energies in GaAs: application to Ga self-diffusion. *Phys. Rev. Lett.* 67:2339–42
61. Van de Walle CG, Laks DB, Neumark GF, Pantelides ST. 1993. First-principles calculations of solubilities and doping limits: Li, Na, and N in ZnSe. *Phys. Rev. B* 47:9425–34
62. Makov G, Payne MC. 1995. Periodic boundary conditions in ab initio calculations. *Phys. Rev. B* 51:4014–22
63. Lany S, Zunger A. 2008. Assessment of correction methods for the band-gap problem and for finite-size effects in supercell defect calculations: case studies for ZnO and GaAs. *Phys. Rev. B* 78:235104
64. Freysoldt C, Neugebauer J, Van de Walle CG. 2009. Fully ab initio finite-size corrections for charged-defect supercell calculations. *Phys. Rev. Lett.* 102:016402
65. Komsa HP, Rantala TT, Pasquarello A. 2012. Finite-size supercell correction schemes for charged defect calculations. *Phys. Rev. B* 86:045112
66. Gali A, Gällström A, Son NT, Janzén E. 2010. Theory of neutral divacancy in SiC: a defect for spintronics. *Mater. Sci. Forum* 645:395–97
67. Gordon L, Janotti A, Van de Walle CG. 2015. Defects as qubits in 3*C*- and 4*H*-SiC. *Phys. Rev. B* 92:045208
68. Christle DJ, Klimov PV, de las Casas CF, Szász K, Ivády V, et al. 2017. Isolated spin qubits in SiC with a high-fidelity infrared spin-to-photon interface. *Phys. Rev. X* 7:021046
69. Szász K, Ivády V, Abrikosov IA, Janzén E, Bockstedte M, Gali A. 2015. Spin and photophysics of carbon-antisite vacancy defect in 4*H* silicon carbide: a potential quantum bit. *Phys. Rev. B* 91:121201
70. Varley JB, Janotti A, Van de Walle CG. 2016. Defects in AlN as candidates for solid-state qubits. *Phys. Rev. B* 93:161201
71. Seo H, Govoni M, Galli G. 2016. Design of defect spins in piezoelectric aluminum nitride for solid-state hybrid quantum technologies. *Sci. Rep.* 6:20803
72. Szállás A, Szász K, Trinh XT, Son NT, Janzén E, Gali A. 2014. Characterization of the nitrogen split interstitial defect in wurtzite aluminum nitride using density functional theory. *J. Appl. Phys.* 116:113702
73. Willardson RK, Weber ER, Stavola M. 1998. *Identification of Defects in Semiconductors*. San Diego, CA: Academic Press

74. Stoneham AM. 2001. *Theory of Defects in Solids: Electronic Structure of Defects in Insulators and Semiconductors*. Oxford, UK: Oxford Univ. Press
75. Lyons JL, Alkauskas A, Janotti A, Van de Walle CG. 2015. First-principles theory of acceptors in nitride semiconductors. *Phys. Status Solid. B* 252:900–8
76. Alkauskas A, Buckley BB, Awschalom DD, Van de Walle CG. 2014. First-principles theory of the luminescence lineshape for the triplet transition in diamond NV centres. *New J. Phys.* 16:073026
77. Dreyer CE, Alkauskas A, Lyons JL, Speck JS, Van de Walle CG. 2016. Gallium vacancy complexes as a cause of Shockley-Read-Hall recombination in III-nitride light emitters. *Appl. Phys. Lett.* 108:141101
78. Huang K, Rhys A. 1950. Theory of light absorption and non-radiative transitions in *F*-centres. *Proc. R. Soc. A* 204:406–23
79. Lax M. 1952. The Franck-Condon principle and its application to crystals. *J. Chem. Phys.* 20:1752–60
80. Goss JP, Jones R, Breuer SJ, Briddon PR, Öberg S. 1996. The twelve-line 1.682 eV luminescence center in diamond and the vacancy-silicon complex. *Phys. Rev. Lett.* 77:3041–44
81. Hossain FM, Doherty MW, Wilson HF, Hollenberg LCL. 2008. Ab initio electronic and optical properties of the NV-center in diamond. *Phys. Rev. Lett.* 101:226403
82. Ma Y, Rohlfing M. 2008. Optical excitation of deep defect levels in insulators within many-body perturbation theory: the *F* center in calcium fluoride. *Phys. Rev. B* 77:115118
83. Alkauskas A, McCluskey MD, Van de Walle CG. 2016. Tutorial: Defects in semiconductors—combining experiment and theory. *J. Appl. Phys.* 119:181101
84. Markham JJ. 1959. Interaction of normal modes with electron traps. *Rev. Mod. Phys.* 31:956–89
85. Alkauskas A, Lyons JL, Steiauf D, Van de Walle CG. 2012. First-principles calculations of luminescence spectrum line shapes for defects in semiconductors: the example of GaN and ZnO. *Phys. Rev. Lett.* 109:267401
86. Kubo R, Toyozawa Y. 1955. Application of the method of generating function to radiative and non-radiative transitions of a trapped electron in a crystal. *Prog. Theor. Phys.* 13:160–82
87. Zhang J, Wang CZ, Zhu ZZ, Dobrovitski VV. 2011. Vibrational modes and lattice distortion of a nitrogen-vacancy center in diamond from first-principles calculations. *Phys. Rev. B* 84:035211
88. Mori-Sánchez P, Cohen AJ, Yang W. 2008. Localization and delocalization errors in density functional theory and implications for band-gap prediction. *Phys. Rev. Lett.* 100:146401
89. Lany S, Zunger A. 2009. Polaronic hole localization and multiple hole binding of acceptors in oxide wide-gap semiconductors. *Phys. Rev. B* 80:085202
90. Dabo I, Ferretti A, Poilvert N, Li Y, Marzari N, Cococcioni M. 2010. Koopmans' condition for density-functional theory. *Phys. Rev. B* 82:115121
91. Deák P, Aradi B, Frauenheim T, Janzén E, Gali A. 2010. Accurate defect levels obtained from the HSE06 range-separated hybrid functional. *Phys. Rev. B* 81:153203
92. Alkauskas A, Dreyer CE, Lyons JL, Van de Walle CG. 2016. Role of excited states in Shockley-Read-Hall recombination in wide-band-gap semiconductors. *Phys. Rev. B* 93:201304
93. Kaduk B, Kowalczyk T, Van Voorhis T. 2012. Constrained density functional theory. *Chem. Rev.* 112:321–70
94. Dederichs PH, Blügel S, Zeller R, Akai H. 1984. Ground states of constrained systems: application to cerium impurities. *Phys. Rev. Lett.* 53:2512–15
95. Wu Q, Van Voorhis T. 2005. Direct optimization method to study constrained systems within density-functional theory. *Phys. Rev. A* 72:024502
96. Gunnarsson O, Lundqvist BI. 1976. Exchange and correlation in atoms, molecules, and solids by the spin-density-functional formalism. *Phys. Rev. B* 13:4274–98
97. Gali A, Fyta M, Kaxiras E. 2008. Ab initio supercell calculations on nitrogen-vacancy center in diamond: electronic structure and hyperfine tensors. *Phys. Rev. B* 77:155206
98. Larsson JA, Delaney P. 2008. Electronic structure of the nitrogen-vacancy center in diamond from first-principles theory. *Phys. Rev. B* 77:165201
99. Delaney P, Greer JC, Larsson JA. 2010. Spin-polarization mechanisms of the nitrogen-vacancy center in diamond. *Nano Lett.* 10:610–14
100. Gali A, Janzén E, Deák P, Kresse G, Kaxiras E. 2009. Theory of spin-conserving excitation of the NV center in diamond. *Phys. Rev. Lett.* 103:186404

101. Ma Y, Rohlfing M, Gali A. 2010. Excited states of the negatively charged nitrogen-vacancy color center in diamond. *Phys. Rev. B* 81:041204
102. Davies G, Hamer M. 1976. Optical studies of the 1.945 eV vibronic band in diamond. *Proc. R. Soc. A* 348:285–98
103. Ivády V, Szász K, Falk AL, Klimov PV, Janzén E, et al. 2016. First principles identification of divacancy related photoluminescence lines in 4H and 6H-SiC. *Mater. Science Forum* 858:322–25
104. von Barth U. 1979. Local-density theory of multiplet structure. *Phys. Rev. A* 20:1693–703
105. Onida G, Reining L, Rubio A. 2002. Electronic excitations: density-functional versus many-body Green's-function approaches. *Rev. Mod. Phys.* 74:601–59
106. Chen W, Pasquarello A. 2015. First-principles determination of defect energy levels through hybrid density functionals and *GW*. *J. Phys. Condens. Matter* 27:133202
107. Surh MP, Chacham H, Louie SG. 1995. Quasiparticle excitation energies for the F-center defect in LiCl. *Phys. Rev. B* 51:7464–70
108. Tiago ML, Chelikowsky JR. 2006. Optical excitations in organic molecules, clusters, and defects studied by first-principles Green's function methods. *Phys. Rev. B* 73:205334
109. Karsai F, Tiwald P, Laskowski R, Tran F, Koller D, et al. 2014. *F* center in lithium fluoride revisited: comparison of solid-state physics and quantum-chemistry approaches. *Phys. Rev. B* 89:125429
110. Rinke P, Schleife A, Kioupakis E, Janotti A, Rödl C, et al. 2012. First-principles optical spectra for *F* centers in MgO. *Phys. Rev. Lett.* 108:126404
111. Bockstedte M, Marini A, Pankratov O, Rubio A. 2010. Many-body effects in the excitation spectrum of a defect in SiC. *Phys. Rev. Lett.* 105:026401
112. Attaccalite C, Bockstedte M, Marini A, Rubio A, Wirtz L. 2011. Coupling of excitons and defect states in boron-nitride nanostructures. *Phys. Rev. B* 83:144115
113. Runge E, Gross EKU. 1984. Density-functional theory for time-dependent systems. *Phys. Rev. Lett.* 52:997–1000
114. Marques MA, Gross EK. 2004. Time-dependent density functional theory. *Annu. Rev. Phys. Chem.* 55:427–55
115. Paier J, Marsman M, Kresse G. 2008. Dielectric properties and excitons for extended systems from hybrid functionals. *Phys. Rev. B* 78:121201
116. Ernzerhof M, Scuseria GE. 1999. Assessment of the Perdew–Burke–Ernzerhof exchange-correlation functional. *J. Chem. Phys.* 110:5029–36
117. Zyubin A, Mebel A, Hayashi M, Chang H, Lin S. 2009. Quantum chemical modeling of photoadsorption properties of the nitrogen-vacancy point defect in diamond. *J. Comput. Chem.* 30:119–31
118. Booth GH, Grüneis A, Kresse G, Alavi A. 2013. Towards an exact description of electronic wavefunctions in real solids. *Nature* 493:365–70
119. Fuchs GD, Dobrovitski VV, Hanson R, Batra A, Weis CD, et al. 2008. Excited-state spectroscopy using single spin manipulation in diamond. *Phys. Rev. Lett.* 101:117601
120. Childress L, Gurudev Dutt MV, Taylor JM, Zibrov AS, Jelezko F, et al. 2006. Coherent dynamics of coupled electron and nuclear spin qubits in diamond. *Science* 314:281–85
121. Ivády V, Szász K, Falk AL, Klimov PV, Christle DJ, et al. 2015. Theoretical model of dynamic spin polarization of nuclei coupled to paramagnetic point defects in diamond and silicon carbide. *Phys. Rev. B* 92:115206
122. Van de Walle CG. 1990. Structural identification of hydrogen and muonium centers in silicon: first-principles calculations of hyperfine parameters. *Phys. Rev. Lett.* 64:669–72
123. Van de Walle CG, Blöchl PE. 1993. First-principles calculations of hyperfine parameters. *Phys. Rev. B* 47:4244–55
124. Blöchl PE. 2000. First-principles calculations of defects in oxygen-deficient silica exposed to hydrogen. *Phys. Rev. B* 62:6158–79
125. Szász K, Hornos T, Marsman M, Gali A. 2013. Hyperfine coupling of point defects in semiconductors by hybrid density functional calculations: the role of core spin polarization. *Phys. Rev. B* 88:075202
126. Gali A. 2009. Identification of individual ^{13}C isotopes of nitrogen-vacancy center in diamond by combining the polarization studies of nuclear spins and first-principles calculations. *Phys. Rev. B* 80:241204

127. Gali A. 2009. Theory of the neutral nitrogen-vacancy center in diamond and its application to the realization of a qubit. *Phys. Rev. B* 79:235210
128. Felton S, Edmonds AM, Newton ME, Martineau PM, Fisher D, et al. 2009. Hyperfine interaction in the ground state of the negatively charged nitrogen vacancy center in diamond. *Phys. Rev. B* 79:075203
129. Bockstedte M, Gali A, Mattausch A, Pankratov O, Steeds JW. 2008. Identification of intrinsic defects in SiC: towards an understanding of defect aggregates by combining theoretical and experimental approaches. *Phys. Status Solid. B* 245:1281–97
130. Szász K, Trinh XT, Son NT, Janzén E, Gali A. 2014. Theoretical and electron paramagnetic resonance studies of hyperfine interaction in nitrogen doped 4H and 6H SiC. *J. Appl. Phys.* 115:073705
131. Carlsson P, Son NT, Gali A, Isoya J, Morishita N, et al. 2010. EPR and ab initio calculation study on the EI4 center in 4*H*- and 6*H*-SiC. *Phys. Rev. B* 82:235203
132. Rondin L, Tetienne J, Hingant T, Roch J, Maletinsky P, Jacques V. 2014. Magnetometry with nitrogen-vacancy defects in diamond. *Rep. Prog. Phys.* 77:056503
133. Kaupp M, Michael B, Malkin VG, eds. 2006. *Calculation of NMR and EPR Parameters: Theory and Applications*. Weinheim, Ger.: John Wiley & Sons
134. Rayson MJ, Briddon PR. 2008. First principles method for the calculation of zero-field splitting tensors in periodic systems. *Phys. Rev. B* 77:035119
135. Bodrog Z, Gali A. 2013. The spin-spin zero-field splitting tensor in the projector-augmented-wave method. *J. Phys. Condens. Matter* 26:015305
136. Ivády V, Simon T, Maze JR, Abrikosov IA, Gali A. 2014. Pressure and temperature dependence of the zero-field splitting in the ground state of NV centers in diamond: a first-principles study. *Phys. Rev. B* 90:235205
137. Doherty MW, Struzhkin VV, Simpson DA, McGuinness LP, Meng Y, et al. 2014. Electronic properties and metrology applications of the diamond NV^- center under pressure. *Phys. Rev. Lett.* 112:047601
138. von Bardeleben HJ, Cantin JL, Csóré A, Gali A, Rauls E, Gerstmann U. 2016. NV centers in 3C, 4H, and 6H silicon carbide: a variable platform for solid-state qubits and nanosensors. *Phys. Rev. B* 94:121202
139. Schreckenbach G, Ziegler T. 1997. Calculation of the *g*-tensor of electron paramagnetic resonance spectroscopy using gauge-including atomic orbitals and density functional theory. *J. Phys. Chem. A* 101:3388–99
140. Pickard CJ, Mauri F. 2002. First-principles theory of the EPR *g* tensor in solids: defects in quartz. *Phys. Rev. Lett.* 88:086403
141. Alkauskas A, Yan Q, Van de Walle CG. 2014. First-principles theory of nonradiative carrier capture via multiphonon emission. *Phys. Rev. B* 90:075202
142. Berland K, Cooper VR, Lee K, Schröder E, Thonhauser T, et al. 2015. van der Waals forces in density functional theory: a review of the vdW-DF method. *Rep. Prog. Phys.* 78:066501
143. Kümmel S, Kronik L. 2008. Orbital-dependent density functionals: theory and applications. *Rev. Mod. Phys.* 80:3–60
144. Bruneval F. 2012. Range-separated approach to the RPA correlation applied to the van der Waals bond and to diffusion of defects. *Phys. Rev. Lett.* 108:256403